ORIGINAL ARTICLE

lajss.org© Latin American Journal of Solids and Structures

www.lajss.org

Study on the penetration performance of shaped charge jet formed by nanocrystalline copper liner

Azhen Zhang[a], Rongxin Li[a], Longfei Xie[b], Ruiqi Wang[a], Junyi Huang[a], Zhenru Gao[a], Yuchun Li[a*], Bo Zhou[b*]

[a] College of Field Engineering, PLA Army Engineering University, Nanjing 210007, China. Email: zazhen1220@163.com; lirongxin2682022@163.com; wrqrich@163.com; huangjunyi357@163.com; gygzr@sina.com; liyuchunmail@sina.com
[b] Xi'an Rare Metal Materials Research Institute Co., Ltd., Xi'an 710006, China. Email: lfeixie@163.com; bozhou23@163.com

* Corresponding author

https://doi.org/10.1590/1679-7825/e8682

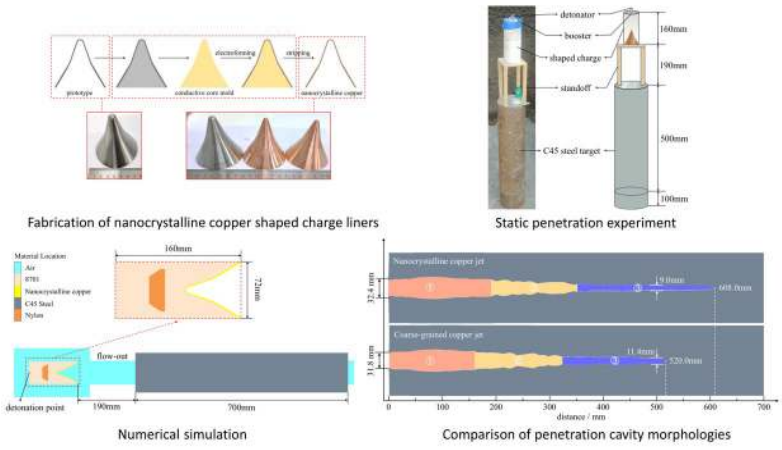
Abstract

Shaped charges, as a core technology in modern weapon systems and engineering breaching applications, achieve high-efficiency penetration through precisely controlled energy release. This capability has become critical for enhancing combat effectiveness and addressing complex engineering challenges. Based on electroforming technology, nanocrystalline copper liners were fabricated. Mechanical properties testing of the nanocrystalline copper material and penetration experiments of shaped charge jets into C45 steel targets were conducted. The Johnson-Cook constitutive model parameters applicable to nanocrystalline copper were obtained through data fitting. Numerical simulations of jet formation and penetration processes for both nanocrystalline and coarse-grained copper liners were conducted utilizing AUTODYN software. The penetration effectiveness of jets from the two types of liners was analyzed based on computational results. The study revealed that the nanocrystalline copper liner exhibits a yield strength of 250 MPa and good plasticity. Compared to the coarse-grained copper liner, the nanocrystalline copper jet demonstrated superior cohesion and continuity, achieving a 13.5% increase in average penetration depth under identical charge configurations and standoff distances. The experimental results exhibited high consistency with the simulation results, with all discrepancies remaining below 10.0%, confirming the accuracy of the fitted material parameters for nanocrystalline copper. These findings provide critical insights for further optimization of nanocrystalline copper in shaped charge design.

Keywords

Nanocrystalline copper, Mechanical properties, Shaped charge, Penetration performance, Numerical simulation

Graphical Abstract



Received april 22, 2025. In revised form june 22, 2025. Accepted july 13, 2025. Available online july 15, 2025.
https://doi.org/10.1590/1679-7825/e8682

Latin American Journal of Solids and Structures. ISSN 1679-7825. Copyright © 2025. This is an Open Access article distributed under the terms of the Creative Commons Attribution License, which permits unrestricted use, distribution, and reproduction in any medium, provided the original work is properly cited.

1 INTRODUCTION

Shaped charges play a crucial role in military defense (Wang et al. 2021, Chen et al. 2024), petroleum extraction (Liu et al. 2023), and blasting demolition (Chai et al. 2023). As the core component of shaped charge structures, the effective length and fracture time of the jet formed by the liner serve as critical indicators of penetration power. Domestic and international studies have demonstrated a strong correlation between the penetration power of metallic liners and their initial grain size (Golaski 1987, Bourne et al. 1993, Wang et al. 1996). Refining the grain size of liner materials can increase the effective continuous jet length, delay jet fracture, and enhance static penetration performance. Oxygen-free high-conductivity (OFHC) copper has become widely adopted due to its material properties and processing cost advantages. However, liners produced by conventional methods typically exhibit grain sizes exceeding tens of micrometers. Further refining the grain size to the nanometer scale could potentially elevate the penetration performance of traditional copper liners.

To achieve the transition of grain size in copper liners from microscale to nanoscale and overcome the limitations of conventional processing methods, the adoption of novel preparation methods becomes essential. Current methods for preparing nanocrystalline metallic materials can be categorized into two approaches: top-down refinement and bottom-up synthesis (Huang et al. 2016). Refinement techniques include severe plastic deformation (SPD) methods (Ebrahimi et al. 2019), however, materials produced by these methods contain significant internal stresses, which can substantially impact the performance of shaped charge liners. Among synthesis methods, such as powder metallurgy (Jiang et al. 2022), chemical vapor deposition (CVD) (Ye et al. 2017), and magnetron sputtering (Xiao et al. 2025), although they offer control over microstructure, they suffer from distinct drawbacks like high porosity, low deposition rates, and prohibitive raw material costs, respectively. These limitations make it difficult to simultaneously meet the demands for manufacturing large-scale, complex components and cost-effectiveness. In contrast, electroforming offers significant advantages (Zhou et al. 2021), including broad material applicability, cost-effectiveness, the ability to produce nanocrystalline materials, and the capability to form complex geometries. Consequently, it stands as the most suitable method for shaped charge liner fabrication.

Research on electroformed liners commenced in the United States in the early 1950s, with batch production capabilities established by the mid-1950s, exemplified by the electroformed copper liners for 105 mm tank gun high-explosive anti-tank (HEAT) projectiles (Sun, 1992). By 2000, collaborative efforts between the University of Toronto (Canada) and Germany led to the development of nanoscale electroformed liners (Wang, 2012). Sun et al. (Sun, 2000) pioneered the advancement of electroformed liners in China, addressing a critical technological gap. Building upon this foundation, further investigations were conducted by Lei (2003, 2010), Li (2009, 2011), Tian (2003), Fan (2007, 2008), and Yang (2010). Their results demonstrate that nanocrystalline liners with distinct preferred growth orientations can be synthesized by modulating electroforming parameters. Compared to conventional liners, electroformed variants exhibit superior yield strength and ultimate tensile strength. Tamer et al. (2017) fabricated 30 mm caliber liners within optimized current density ranges and conducted penetration experiments against armored targets. Results indicated a 22.7% enhancement in penetration depth for the optimized electroformed copper liners. However, this study presented only a superficial comparison of penetration outcomes without in-depth mechanistic analysis. In summary, extant research primarily focuses on optimization of electroforming process parameters, microstructural characterization, and quasi-static mechanical property testing. Nevertheless, systematic investigations into mechanical behavior spanning quasi-static to high-strain-rate regimes remain relatively scarce. Furthermore, studies on critical aspects such as explosive-liner interaction, shaped charge jet formation characteristics, and terminal ballistic effects are insufficiently comprehensive. Consequently, as a pivotal structural component in shaped charges, imperative research directions should encompass jet formation mechanisms and penetration efficacy of electroformed nanocrystalline liners.

This study focuses on electroformed nanocrystalline copper liners. Systematic quasi-static tensile testing and split Hopkinson tensile bar (SHTB) experiments are conducted to characterize their stress-strain responses across quasi-static to high-strain-rate regimes under varying temperatures. Mechanical test data are employed to calibrate key parameters of the Johnson-Cook constitutive model applicable to wide strain rate ranges. This establishes a dynamic response model for nanocrystalline copper liners subjected to detonation loading. Through an integrated experimental and numerical simulation approach, performance enhancements relative to conventional copper liners are quantitatively evaluated in terms of penetration depth and entrance diameters. The findings provide a scientific basis and dataset for design optimization and performance prediction of electroformed nanocrystalline copper liners.

2 EXPERIMENTAL SECTION

2.1 Specimen preparation

The nanocrystalline copper tensile specimens and shaped charge liners fabricated via micro-electroforming technology exhibited a density of approximately 8.9 g·cm^{-3} and a relative density of 99.5%. The fabrication process is illustrated in Figure 1.

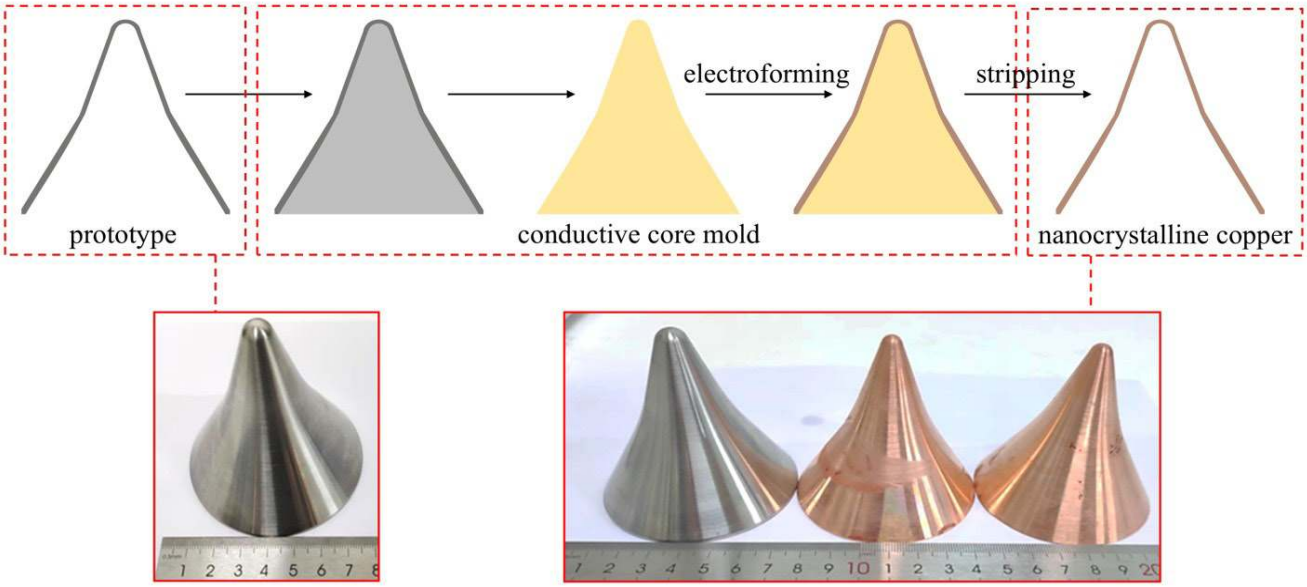


Figure 1 Fabrication process flow chart of nanocrystalline copper shaped charge liner

(1) Fabrication of conductive core mold. The prototype dimensions of tensile specimens and shaped charge liners are shown in Figure 2.

(2) Electroforming of nanocrystalline copper specimens. The conductive mandrel was fixed with metal wires and immersed in the electroforming bath as the cathode, with pure copper serving as the anode. Electrochemical deposition was conducted utilizing an electrochemical workstation. The process continued until the mandrel cavity was fully filled with deposited metal ions. The mandrel was then removed, ultrasonically cleaned in deionized water, and oven-dried.

(3) Stripping and post-processing of nanocrystalline copper specimens. Manual stripping was employed to extract the specimens from the mandrel cavity. Subsequent surface treatments, including grinding and polishing, were executed to obtain the nanocrystalline copper specimens.

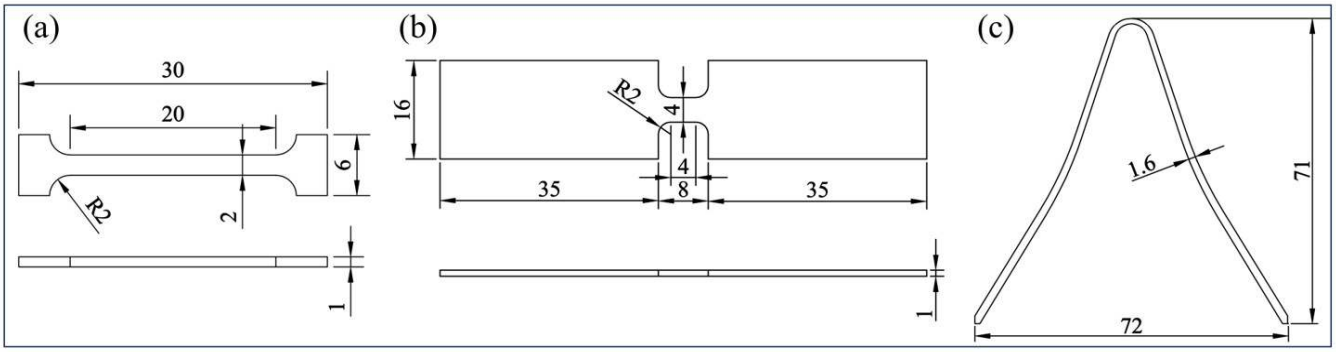


Figure 2 Schematic diagram of test specimen dimensions(unit: mm): (a) quasi-static tensile test specimen; (b) dynamic tensile test specimen; (c) shaped charge liner specimen

2.2 Microstructure testing

The intrinsic microstructural features of the electroformed nanocrystalline copper specimens were characterized via an FEI Talos F200X G2 transmission electron microscope (TEM).

2.3 Quasi-static and dynamic tensile testing

Quasi-static tensile tests were performed on the tensile specimens utilizing an electronic universal testing machine (LD 26.105, Li-SHI Instrument Co., Ltd., China). The specimen dimensions are shown in Figure 2(a). The crosshead speed was set to 2 mm·min^{-1}, and two sets of tests were conducted. Dynamic mechanical properties were evaluated utilizing a split Hopkinson tensile bar (SHTB) apparatus (ZDSHTB-20, ZONE-DE Electro-Mechanical Equipment Co., Ltd., China). The specimen dimensions are provided in Figure 2(b), and a schematic of the experimental setup is illustrated in Figure 3. Dynamic tensile tests were carried out under room-temperature conditions at strain rates ranging from 1000 to 3500 s^{-1}, maintaining approximately the same high strain rate regime, with additional tests conducted at 300 K, 395 K, and 475 K.

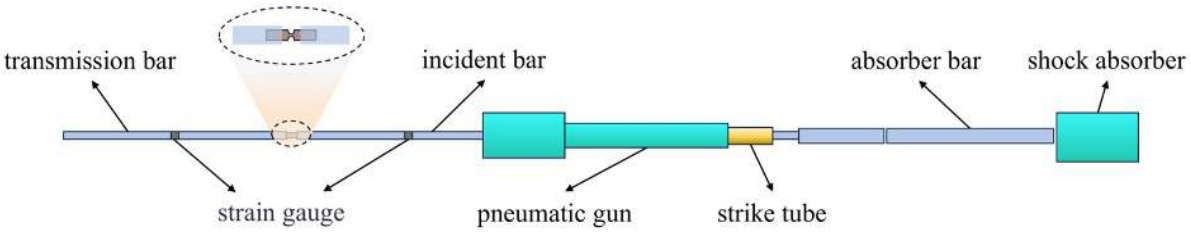


Figure 3 Schematic diagram of the SHTB experimental setup

2.4 Static penetration experiment

Static penetration experiments were conducted to evaluate the penetration and damage effects of electroformed nanocrystalline copper liners on C45 steel targets. Based on previous experimental conditions for coarse-grained copper liners, the shaped charge configuration and static penetration test setup are illustrated in Figure 4. The shaped charge assembly consisted of a booster charge, auxiliary charge, wave shaper, main charge, and liner. Both the main and auxiliary charges were composed of JH-2 (8701) explosive pressed a density of 1.69 g·cm^{-3}. The wave shaper was fabricated from nylon with a density of 1.14 g·cm^{-3}, and the liner was made of nanocrystalline copper with a density of 8.9 g·cm^{-3}. The charge assembly was mounted on a 190 mm-high wooden stand, beneath which two cylindrical C45 steel targets (diameter: 130 mm; thicknesses: 500 mm and 100 mm) were positioned. Central initiation was employed to detonate the explosive. Upon detonation, the initial divergent detonation wave was redirected by the wave shaper, forming a convergent detonation wave. This configuration enhanced the collapse velocity of the liner, thereby generating a high-velocity jet (Huang et al. 2021).

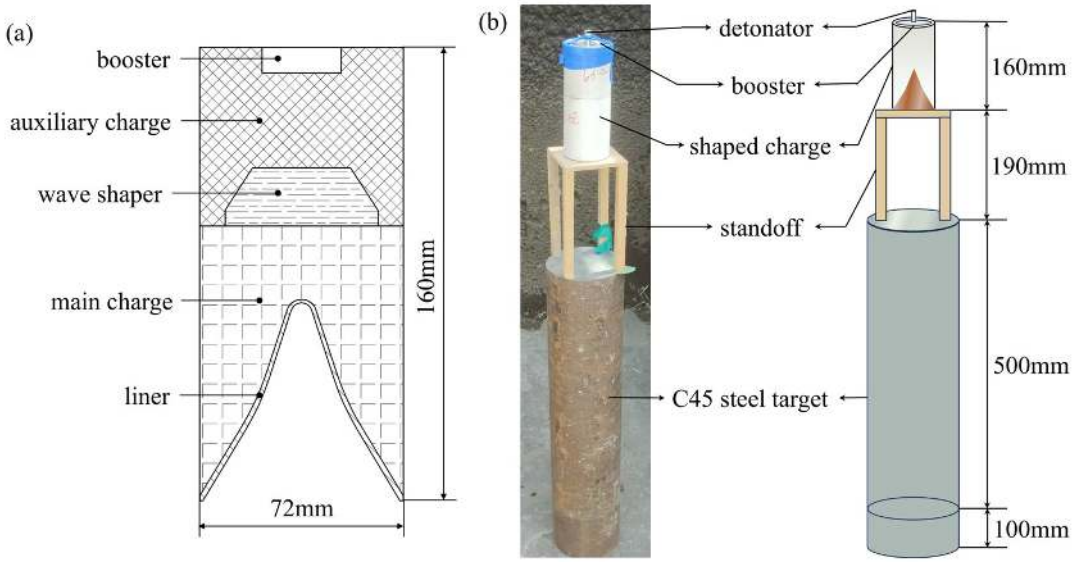


Figure 4 Schematic diagram of the experimental setup:(a) shaped charge configuration; (b) test layout

3 RESULTS AND DISCUSSION

3.1 Microstructural characteristics

TEM observations were conducted to investigate the microstructure of the electroformed nanocrystalline copper specimens, focusing on crystal defects and characterization of grain size and morphology. Figure 5 presents the bright-field micrograph, Selected Area Electron Diffraction (SAED) pattern, and corresponding grain size distribution histogram of the nanocrystalline copper. As shown in Figure 5(a), the bright-field micrograph reveals predominantly equiaxed grain morphology, with the SAED pattern clearly indexed for the (111), (200), (220), and (311) planes, confirming the FCC structure and polycrystalline nature. Figure 5(b) clearly displays the configuration and distribution of twin boundaries. Figure 5(c) provides a magnified view of the microstructure, with a further enlarged inset in the upper-right corner detailing grain boundary features. Statistical analysis of 300 grains from bright-field images yielded the grain size distribution shown in Figure 5(d). The histogram, now including labeled relative frequency values and a fitted Gaussian distribution curve (blue line), demonstrates a mean grain size of 34.37±0.72 nm (R^2=0.9897). The distribution shows inhomogeneity, with ultra-fine grains coexisting in the matrix. The average grain size in homogeneous regions determined directly from micrographs is 56 nm, consistent with SAED results where larger diffraction spots (indicative of the ultra-fine grains) are embedded within diffraction rings (corresponding to the nanocrystalline).

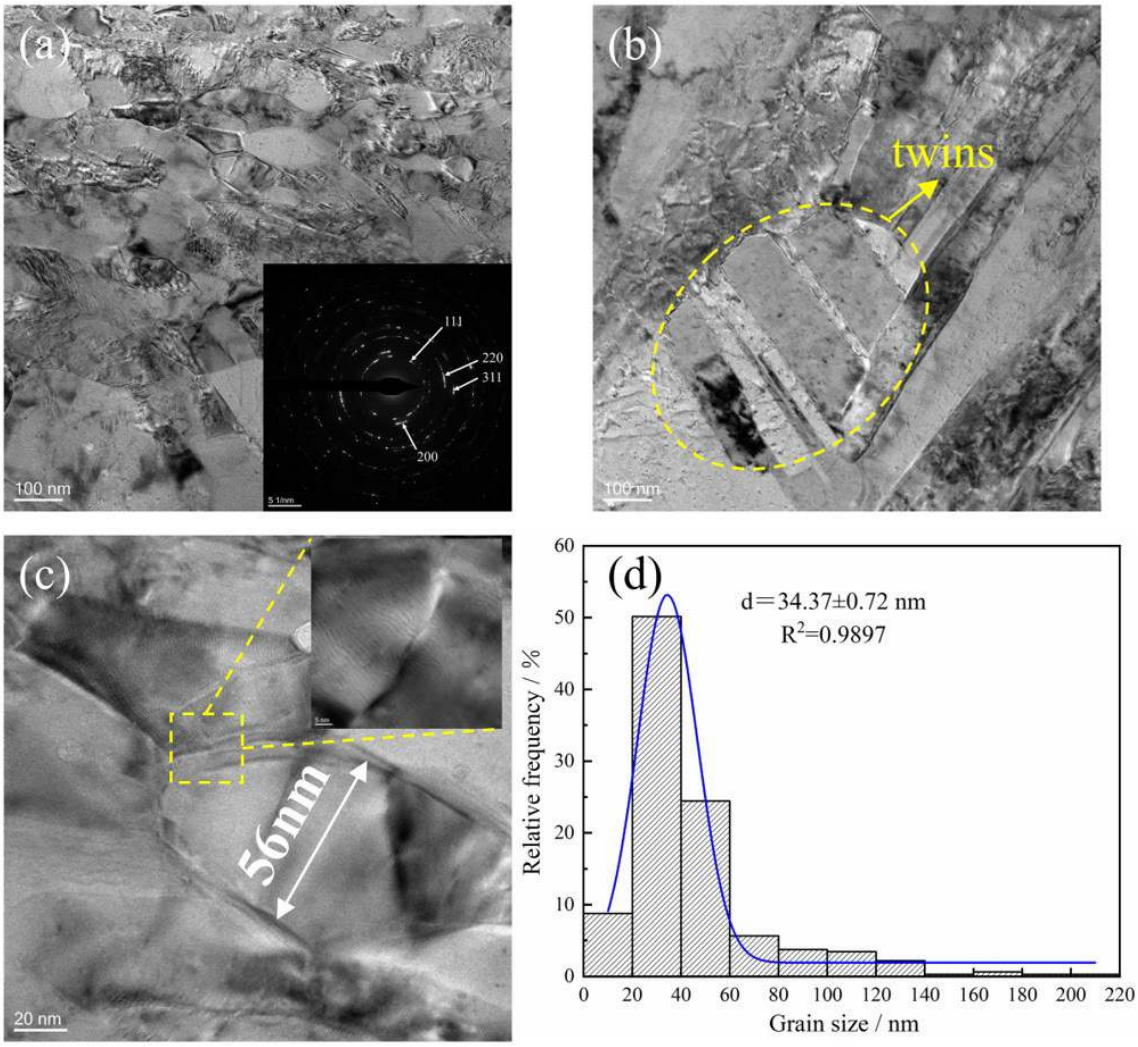


Figure 5 TEM micrographs of electroformed nanocrystalline copper: (a) bright-field TEM images with SAED patterns; (b) twins; (c) locally magnified TEM images; (d) grain size distribution

3.2 Mechanical testing results and analysis

3.2.1 Quasi-static mechanical properties

The true stress-strain curves of two specimen groups under quasi-static tensile loading are shown in Figure 6, demonstrating high consistency between the datasets. Averaging the results from both groups, the quasi-static yield strength (0.2% offset strain) of the nanocrystalline copper was determined as 250 MPa, with an ultimate tensile strength of 340 MPa and elongation of approximately 15%. While the yield and tensile strengths of the nanocrystalline copper exceed those of conventional oxygen-free copper, its ductility is comparatively reduced. According to the Hall-Petch relationship (Li et al. 2025): $\sigma_y=\sigma_0+kd^{-1/2}$, where σ_y is the yield stress, d is the grain size, σ_0 is the frictional stress and k is the constant. Theoretically, the strength of a material is inversely proportional to the square root of its grain size. This inverse relationship suggests that nanocrystalline materials should exhibit significantly higher strength compared to their conventional polycrystalline counterparts. However, experimental observations indicated that the synthesized nanocrystalline copper exhibited no substantial strength enhancement. Lei et al. (2004) provided experimental evidence elucidating the limitations of the Hall-Petch relationship in electroformed nanocrystalline materials. The breakdown originates from the Hall-Petch model's fundamental assumption of dislocation pile-up mechanisms, which cease to operate as grain dimensions approach equilibrium dislocation spacing. Under these conditions, restricted dislocation nucleation and motion occur due to limited intragranular volume available for pile-up development. As shown in Figure 5(d), the grain size distribution includes a fraction of grains exceeding 100 nm. The observed strength enhancement through grain refinement indicates limited validity of the Hall-Petch relationship, while the predominance of grain boundary-mediated deformation in finer-grained structures causes progressive departure from classical Hall-Petch predictions.

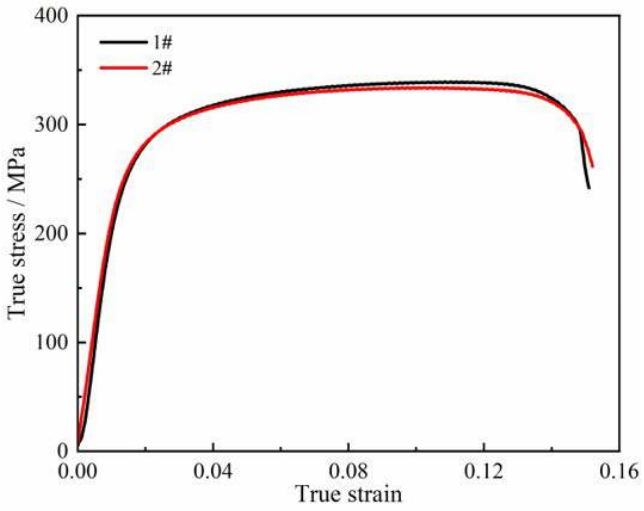


Figure 6 True stress-strain curves under quasi-static tensile loading

Figure 6 further reveals distinct plastic deformation stages in the nanocrystalline copper, potentially associated with twin boundaries. Twin boundaries may function as dislocation nucleation sites, thereby influencing deformation mechanisms. During the plastic deformation stage, true stress progressively rises from the yield point (250 MPa) to 340 MPa, accompanied by pronounced plastic flow. This phenomenon originates from the limited dislocation storage capacity at twin boundaries, causing rapid dislocation depletion. Subsequent deformation transitions to grain boundary sliding or twin boundary migration, ultimately manifesting as plastic flow behavior (Wang et al. 2010). Although nanocrystalline copper exhibits lower elongation than coarse-grained copper, its plastic flow during deformation indicates uniform shape adaptation under external loading. Consequently, from a plastic flow perspective, this material demonstrates good plasticity for liner applications. This plasticity enables delayed jet fracture during shaped charge jet formation, allowing sufficient jet elongation to enhance penetration depth.

3.2.2 Dynamic mechanical properties

The dynamic tensile test results are presented in Figure 7(a), illustrating the true stress-strain relationships of nanocrystalline copper under four strain rates (1200 s^{-1}, 1700 s^{-1}, 2200 s^{-1}, and 3100 s^{-1}). A bilinear model (Huang et al.

2016) was employed to determine the yield strengths at these strain rates, as summarized in Table 1 Compared to quasi-static tensile results, the material exhibits significant strain rate strengthening effects: the yield strength increases from 250 MPa (quasi-static) to 510 MPa (dynamic), with both dynamic yield strength and elongation progressively enhancing as strain rate rises.

Table 1 Yield strengths of nanocrystalline copper under different strain rates

Strain rate/s^{-1}	0.001	1200	1700	2200	3100
Yield strength/MPa	250	459	478	505	510

The grain size of the nanocrystalline copper predominantly ranges between 20 nm and 60 nm, where conventional dislocation multiplication mechanisms are constrained. Plastic deformation primarily relies on dislocation nucleation near grain boundaries. Under thermally activated mechanisms (Zaretsky, 2025), the strain rate and temperature obey the relationship: $\dot{\varepsilon} \propto \exp(-\Delta G/kT)$, where $\dot{\varepsilon}$ is strain rate, ΔG is the activation energy, T is the temperature and k is the Boltzmann constant. At high strain rates, dislocation nucleation requires higher energy input, while insufficient thermal activation time leads to elevated yield strength. While grain boundary activity predominantly governs deformation under high strain rates, increased resistance to boundary migration facilitates concurrent strength enhancement and preservation of flow characteristics.

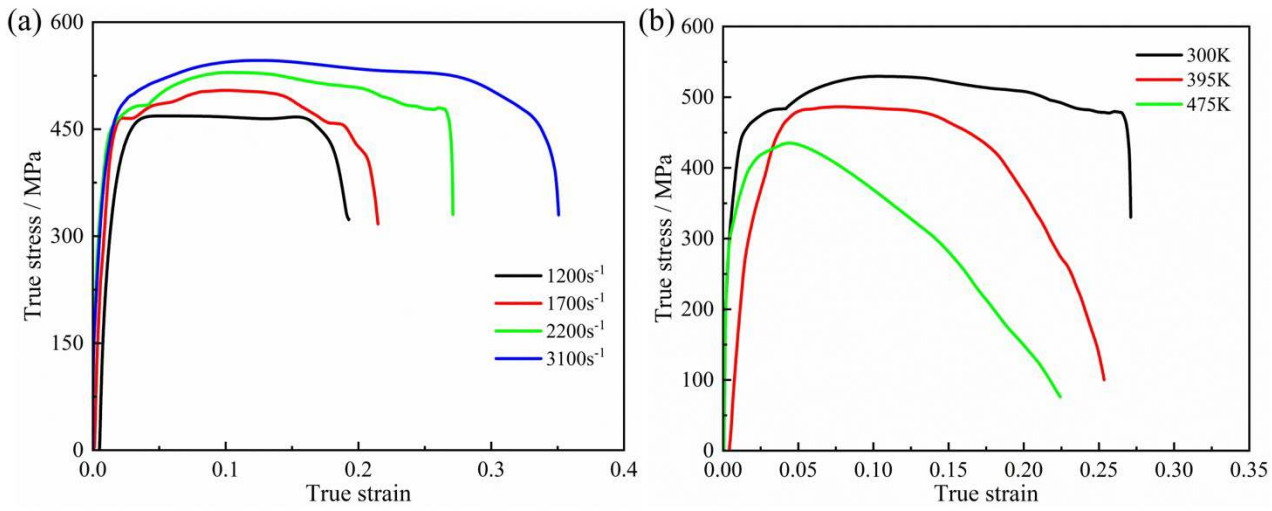


Figure 7 True stress-strain curves under dynamic tensile loading: (a) different strain rates; (b) different temperatures

Dynamic tensile tests were conducted at approximately the same high strain rate (reference strain rate: 2200 s^{-1}) under temperatures of 395 K and 475 K, with results shown in Figure 7(b). As temperature increases, the peak stress of the specimens gradually decreases, demonstrating a pronounced thermal softening effect. At 300 K, the specimens exhibit higher strength, maintaining relatively elevated stress levels throughout the test range and undergoing significant plastic deformation prior to fracture. This indicates superior strength and plastic deformation capacity at lower temperatures. However, at elevated temperatures (395 K and 475 K), stress levels decline progressively, and post-peak stress reduction accelerates. Enhanced thermal activation at high temperatures promotes grain boundary migration rates and reduces the critical resolved shear stress for dynamic recrystallization, thereby lowering the material's flow stress (Li et al. 2024). Concurrently, high-temperature conditions facilitate strain localization through grain boundary sliding, inducing premature microcrack nucleation and reduced elongation.

3.2.3 Determination of constitutive model parameters

Constitutive model parameters can accurately describe the flow stress relationship of materials, making their determination critically important. The Johnson-Cook (J-C) constitutive model incorporates strain hardening, strain rate strengthening effects, and thermal softening effects. It is widely applied in explosion and impact fields due to its simple formulation, clear physical interpretation of each term, and relative ease of parameter acquisition (Li et al. 2024, Gao et al. 2024). Therefore, this study combines the results of quasi-static and dynamic tensile tests to fit the parameters of the J-C constitutive model for nanocrystalline copper. The J-C constitutive model is expressed as follows:

$$\sigma_y = (A + B\varepsilon_{eq}^n)(1 + C\ln\dot{\varepsilon}^*)(1 - T^{*m}) \tag{1}$$

Where σ_y is the von Mises flow stress (MPa); ε_{eq} is the equivalent plastic strain; $\dot{\varepsilon}^*=\dot{\varepsilon}/\dot{\varepsilon}_0$ is the dimensionless plastic strain rate, where $\dot{\varepsilon}$ is the equivalent plastic strain rate (s^{-1}) and $\dot{\varepsilon}_0$ is the reference strain rate (s^{-1}), taken as 10^{-3} s^{-1} (quasi-static condition); $T^*=(T-T_r)/(T_m-T_r)$ is the dimensionless temperature term, where T_r is the reference temperature (typically room temperature, K), and T_m is the melting temperature of the material under normal conditions (K); A is the yield stress at the reference temperature and strain rate (MPa); B is the strain hardening coefficient (MPa); n is the strain hardening exponent; C is the strain rate strengthening coefficient; m is the thermal softening exponent.

The parameters A, B, and n can be determined by fitting the true stress-strain curve obtained under quasi-static conditions at room temperature. In this case, $\dot{\varepsilon}^*=1$, $T^*=0$, simplifying Equation (1) to:

$$\sigma_y = A + B\varepsilon_{eq}^n \tag{2}$$

At the initial yield point ($\varepsilon_{eq}=0$), the parameter A corresponds directly to the yield stress. For instance, A=250 MPa (as derived from experimental data). To solve for B and n, Equation (2) is linearized by taking the natural logarithm of both sides:

$$\ln(\sigma_y - A) = \ln B + n\ln\varepsilon_{eq} \tag{3}$$

The true stress-strain relationship under quasi-static conditions is transformed into a linear correlation expressed as $\ln(\sigma_y-A)$-$\ln\varepsilon_{eq}$, where the slope corresponds to the strain-hardening exponent n and the intercept represents $\ln B$. As shown in Figure 8(a), the fitting results yield B = 344 MPa, n = 0.51。

When the equivalent plastic strain ε_{eq} = 0, the relationship between the yield stress and the strain rate at room temperature is as follows:

$$\sigma_y = A(1 + C\ln\dot{\varepsilon}^*) \tag{4}$$

Through mathematical transformation, the following relationship is derived:

$$(\sigma_y / A) - 1 = C\ln\dot{\varepsilon}^* \tag{5}$$

Under quasi-static conditions, the strain rate serves as the reference strain rate, with a yield strength A=250 MPa. At this point, $\ln\dot{\varepsilon}^*=0$ and $(\sigma_y/A)-1=0$. Based on the yield strengths obtained at different strain rates under room temperature, the transformed relationship is presented in Figure 8(b).

Using 2200 s^{-1} as the reference strain rate, the parameter m can be determined from the temperature-dependent yield strengths under dynamic loading conditions. The equation assumes the following form:

$$\sigma_y = A(1 - T^{*m}) \tag{6}$$

Through mathematical transformation, the following relationship is derived:

$$\ln(1 - \sigma_y / A) = m\ln T^* \tag{7}$$

The fitting result for Equation (7) is shown in Figure 8(c).

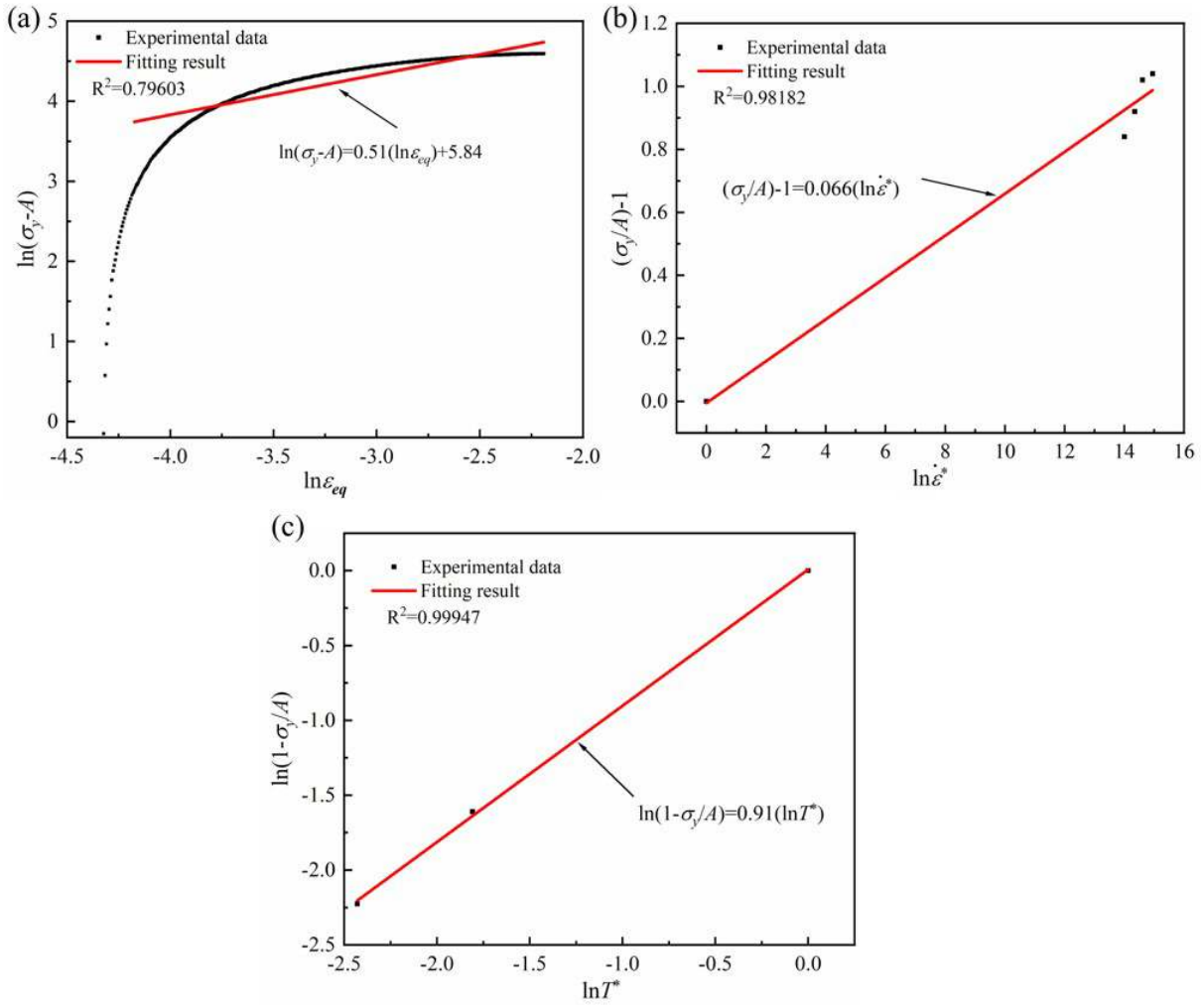


Figure 8 Johnson-Cook constitutive model parameter fitting curves: (a) fitting of parameters B & n; (b) fitting of parameter C; (c) fitting of parameter m

The parameters of the J-C constitutive equation for nanocrystalline copper are determined through fitting, as listed in Table 2. The J-C constitutive equation for nanocrystalline copper can be expressed as:

$$\sigma_y = (250 + 344\varepsilon_{eq}^{0.51})(1 + 0.066\ln\dot{\varepsilon}^*)(1 - T^{*0.91}) \tag{8}$$

Table 2 Parameters of J-C constitutive equation for nanocrystalline copper material

ρ/g·cm^{-3}	A/MPa	B/MPa	n	C	m	$\dot{\varepsilon}_0$/s^{-1}
8.9	250	344	0.51	0.066	0.91	0.001

3.3 Results and analysis of static penetration experiments

3.3.1 Penetration damage results

The penetration damage effects of the nanocrystalline copper shaped charge jet on steel targets are shown in Figure 9. Figures. 9(a), 9(b), and 9(c) present the results from Experiment I, while Figures. 9(d), 9(e), and 9(f) correspond to Experiment II. The shaped charge jet formed relatively regular circular perforations in the steel targets. In both experiments, the first steel target section (500 mm) was fully penetrated, and the jet continued to penetrate the second steel target section (100 mm). In Experiment I, the entrance diameter (D_{en}) of the first target section is 34.0 mm, the exit diameter (D_{ex}) is 8.9 mm, the entrance diameter of the second target section is 9.2 mm, and the penetration depth (P) of the second target section is 83.0 mm. In Experiment II, the entrance diameter of the first target section is 33.0 mm,

the exit diameter is 8.2 mm, the entrance diameter of the second target section is 8.8 mm, and the penetration depth of the second target section is 94.0 mm. Significant copper residue was observed on the rear surface of the first target section and the front surface of the second target section in both experiments, indicating mass loss of the jet during the penetration process. The entrance diameter of the second target section slightly exceeded the exit diameter of the first target section. This suggests that a portion of the jet energy was consumed in expanding the aperture after penetrating the first target, while the remaining energy drove subsequent jet penetration into the second target.

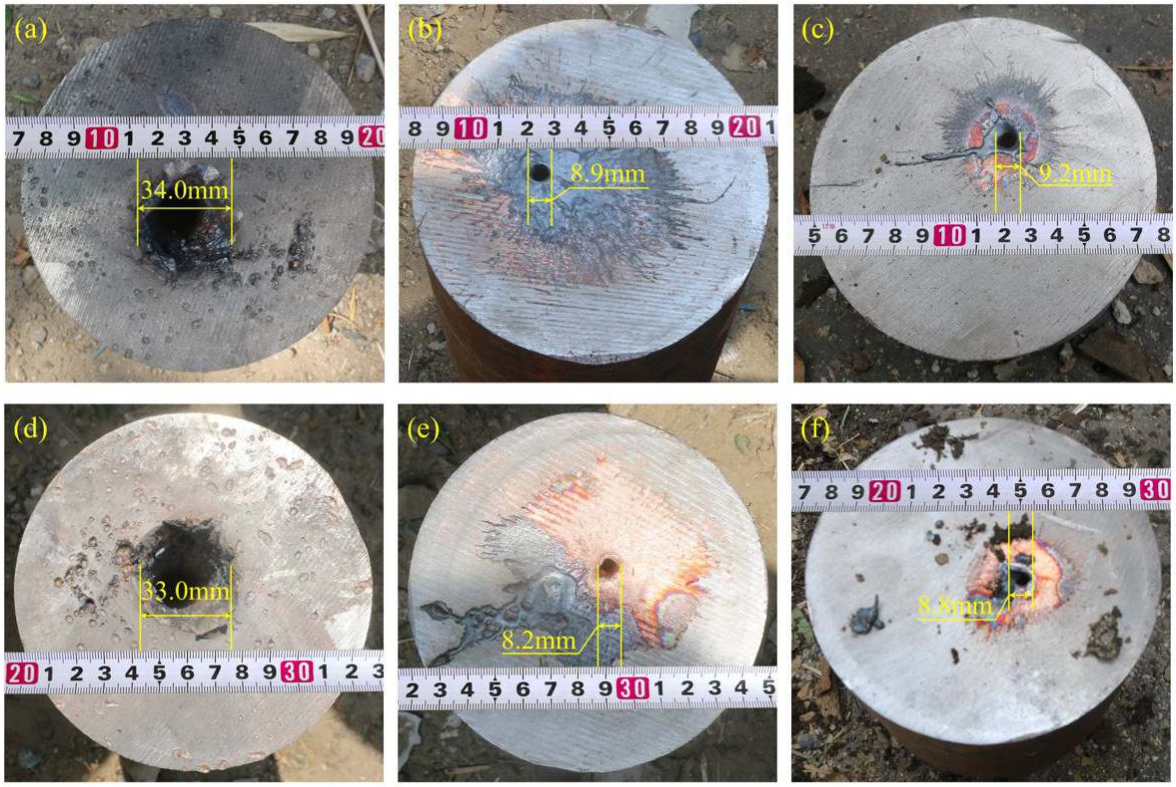


Figure 9 Penetration damage results of the nanocrystalline copper jet: (a) front side of the first target section in Experiment I; (b) rear side of the first target section in Experiment I; (c) front side of the second target section in Experiment I; (d) front side of the first target section in Experiment II; (e) rear side of the first target section in Experiment II; (f) front side of the second target section in Experiment II

As shown in Figure 10, the penetration damage results of the coarse-grained copper liner with identical charge configuration on C45 steel targets at a standoff distance of 190 mm. Figure 10(a) presents the results of Experiment III, where the entrance diameter of the first steel target segment is 43.0 mm, the exit diameter is 12.0 mm, and the total penetration depth is 515.0 mm. Figure 10(b) shows the results of Experiment IV, where the entrance diameter of the first steel target segment is 27.0 mm, the exit diameter is 9.0 mm, and the total penetration depth is 522.0 mm.

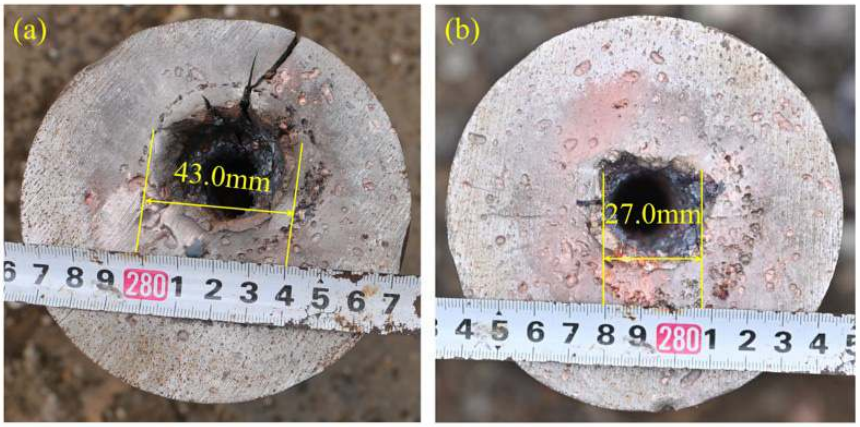


Figure 10 Penetration damage results of the coarse-grained copper jet: (a) Experiment III; (b) Experiment IV

The average entrance diameter ($\overline{D}$) and average penetration depth ($\overline{P}$) from the four experimental groups are summarized in Table 3 Under identical standoff distances, nanocrystalline and coarse-grained copper liners demonstrated comparable entrance diameters. Notably, the nanocrystalline liner achieved a 13.5% greater penetration depth relative to its coarse-grained counterpart, revealing enhanced penetration performance through grain refinement.

Table 3 Comparative penetration performance

Material	D_{en}/mm	$\overline{D}$ /mm	P/mm	$\overline{P}$ /mm
Nanocrystalline copper	34.0	33.5	583.0	588.5
	33.0		594.0	
Coarse-grained copper	43.0	35.0	515.0	518.5
	27.0		522.0	

3.3.2 Numerical simulation study

AUTODYN, as a nonlinear dynamics software, has been validated in multiple studies for its capability to simulate shaped charge phenomena (Li et al. 2024, Dou et al. 2025). It can accurately model the penetration process of shaped charge jets into steel targets. The software incorporates various material models and equations of state (EOS), such as the Johnson-Cook constitutive model and Grüneisen EOS, which precisely describe the dynamic mechanical behavior of metals under high-temperature, high-pressure, and high-strain-rate conditions. These features are critical for simulating material responses during jet penetration. Based on the mechanical property tests of nanocrystalline copper and static penetration experiments of nanocrystalline copper liners, this study conducts numerical simulations of nanocrystalline copper jet penetration into C45 steel targets.

The shaped charge structure and steel target are axisymmetric. To simplify the computational process, a 2D axisymmetric model was established according to the static penetration experimental setup, as shown in Figure 11. The explosive collapse forming the jet involves large deformations and multi-material interactions. Therefore, multi-material Eulerian algorithm was applied to the shaped charge and air domains. Lagrangian algorithm was used for the steel target. Fluid-structure interaction (FSI) algorithm coupled the two domains. Considering the liner wall thickness, computational accuracy, and efficiency, a uniform grid size of 0.3 mm × 0.3 mm was adopted in critical regions, including the shaped charge structure and along the jet formation and penetration paths. In other regions, the grid size was gradually increased. To simulate an infinite air domain, a flow-out boundary condition was applied to the air domain boundaries. The initiation method was set to point detonation, and the computational time was fixed at 600 μs.

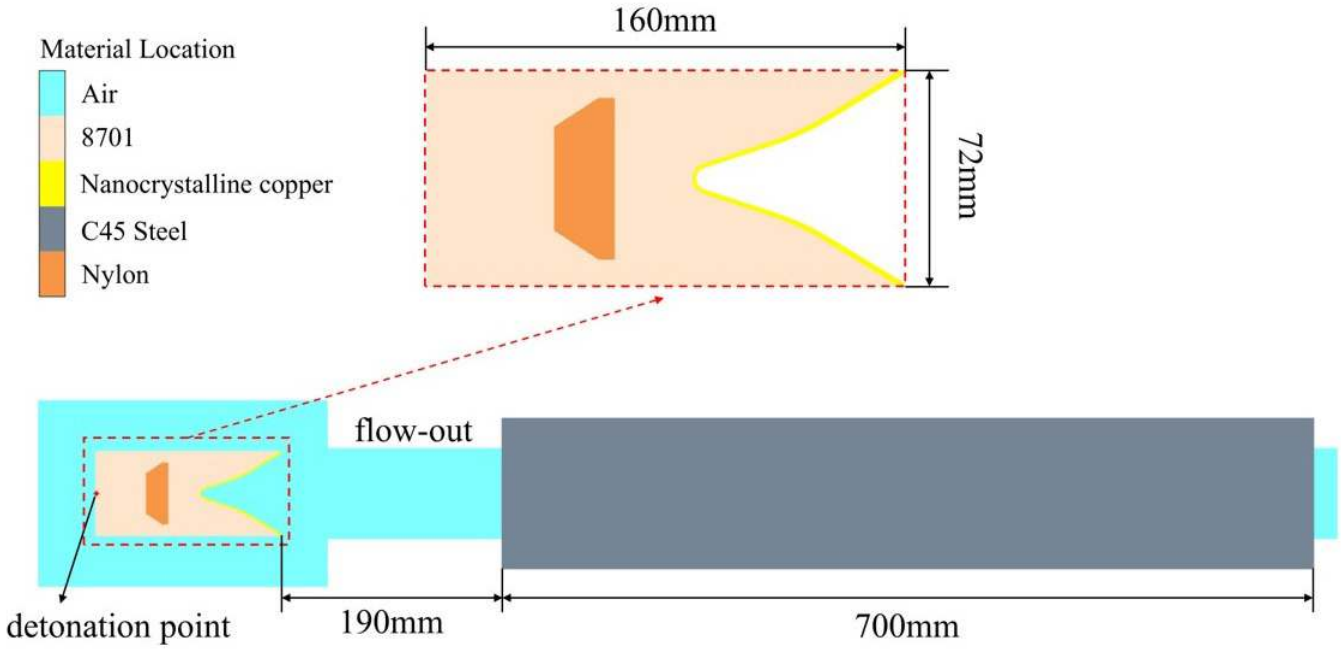


Figure 11 2D axisymmetric numerical model configuration

The Grüneisen shock EOS is an empirical model used to describe material behavior under shock compression conditions. It is widely applied to simulate the mechanical response of materials subjected to extreme environments involving high temperatures, high pressures, and high strain rates. Derived from the Rankine-Hugoniot equations, this equation characterizes the discontinuous changes in material state parameters across a shock wave propagating through a medium. For many fluids and solids, when the pressure exceeds a critical threshold, an empirical linear relationship exists between the shock wave velocity (U_s) and the particle velocity (u_p) ahead of the shock front:

$$U_s = C_0 + Su_p \tag{9}$$

Where C_0 is the bulk sound speed of the material under ambient conditions (km·s^{-1}); S is the linear Hugoniot slope coefficient. This empirical relationship forms the basis for the Grüneisen shock EOS, which is expressed as:

$$p = p_H + \gamma\rho(e - e_H) \tag{10}$$

Where p and p_H represent the pressure of the compressed solid material and the Hugoniot pressure, respectively (Pa); γ is the Grüneisen coefficient of the material; ρ is the material density (g·cm^{-3}); e and e_H represent the energy of the compressed solid material and the Hugoniot energy, respectively (J·kg^{-1}).

Since shock compression experiments were not conducted on the nanocrystalline copper material, the Grüneisen shock EOS parameters were referenced from fine-grained pure copper data in literature (Yan et al. 2017), as summarized in Table 4.

Table 4 Grüneisen shock EOS parameters for liner material (Yan et al. 2017)

C_0/km·s^{-1}	S	γ
4.007	1.485	2.07

The numerical simulation model for the C45 steel target employs the J-C constitutive model and Grüneisen shock EOS. Due to the well-established research on C45 steel material, parameters from reference (Guo et al. 2019) are adopted, as summarized in Table 5.

Table 5 Material parameters for C45 steel (Guo et al. 2019)

ρ/g·cm^{-3}	A/MPa	B/MPa	n	C	m	C_0/km·s^{-1}	S	γ	T_{melt}/K
7.83	792	510	0.26	0.06	1.03	4.57	1.49	2.17	1793

The Jones-Wilkins-Lee (JWL) EOS is widely used in numerical simulations of explosive detonation and explosive-driven processes. Its general form is:

$$p = A(1 - \frac{\omega}{R_1 V})e^{-R_1 V} + B(1 - \frac{\omega}{R_2 V})e^{-R_2 V} + \frac{\omega E_0}{V} \tag{11}$$

Where p is the pressure of detonation products (GPa); E_0 is the initial specific internal energy (J·kg^{-1}); V is the relative volume; A、B、R_1、R_2 and ω are material constants. The material parameters of the 8701 explosive are given in Table 6.

Table 6 Material parameters for 8701 explosive (Hong et al. 2024)

ρ/g·cm^{-3}	D/m·s^{-1}	P_{CJ}/GPa	A/GPa	B/GPa	R_1	R_2	ω	E_0/J·kg^{-1}
1.69	8425	29.5	8.524	0.18	4.6	1.3	0.38	6.04×10^6

The ideal gas EOS is used to describe air, and its expression is as follows:

$$p_A = (\gamma - 1)\rho_A E_A \tag{12}$$

Where p_A is the pressure; γ = 1.4 is the gas constant; the density ρ_A=1.225×10^{-3} g·cm^{-3}; and the specific internal energy E_A=2.068×10^5 J·kg^{-1}。

The wave shaper material (nylon) is described using the Von Mises strength model and Shock EOS, with main parameters listed in Table 7.

Table 7 Material parameters for wave shaper (Zhang et al. 2023)

ρ/g·cm^{-3}	G/GPa	σ_Y/MPa	C_0/km·s^{-1}	S	γ
1.14	3.68	50	2.29	1.63	0.87

Numerical simulations clearly capture the dynamic stretching process of shaped charge jets after formation, which aligns with the Pugh-Eichelberger-Rostoker (PER) unsteady state theory (Pugh et al. 1952) serving as the theoretical foundation for this process. The core principle of this theory states that the collapse velocity of liner micro-elements varies from the apex to the base, resulting in velocity gradients within the jet consistent with observed phenomena. Figure 12 illustrates the liner collapse process and velocity relationships at key points, where α denotes the liner half-cone angle, β is the collapse angle, δ is the deflection angle, and V_0, V_1, V_2 represent the collapse velocity, stagnation velocity, and flow velocity in the moving coordinate system, respectively.

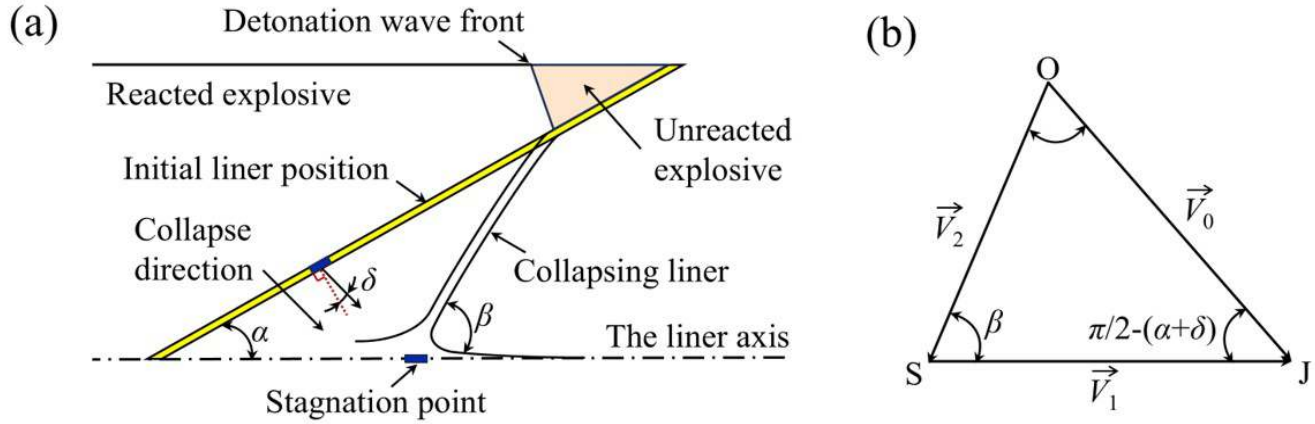


Figure 12 Schematic of the jet formation process: (a) collapse process of the liner; (b) velocity relationship

According to the PER theory, V_1 and V_2 can be obtained by

$$V_1 = \frac{V_0 \cos\left[\beta - (\alpha + \delta)\right]}{\sin\beta} \tag{13}$$

$$V_2 = \frac{V_0 \cos(\alpha + \delta)}{\sin\beta} \tag{14}$$

Respectively, the velocities of the jet (V_j) and slug (V_s) can be written as

$$V_j = V_1 + V_2 = V_0 \csc\frac{\beta}{2}\cos\left(\alpha + \delta - \frac{\beta}{2}\right) \tag{15}$$

$$V_s = V_1 - V_2 = V_0 \sec\frac{\beta}{2}\sin\left(\alpha + \delta - \frac{\beta}{2}\right) \tag{16}$$

Based on conservation of mass and momentum, the mass expressions for the jet (m_j) and slug (m_s) are derived as:

$$\frac{\mathrm{d}m_j}{\mathrm{d}m} = \sin^2\frac{\beta}{2} \tag{17}$$

$$\frac{\mathrm{d}m_s}{\mathrm{d}m} = \cos^2\frac{\beta}{2} \tag{18}$$

Numerical simulation results visually validate the jet formation and stretching characteristics described by PER theory. As shown in Figure 13, at 14 μs the detonation wave reaches the liner apex and initiates compressive deformation. At 20 μs, liner micro-elements accelerate along the collapse direction toward the axis, converging at the PER theory defined stagnation point where they separate into jet and slug according to momentum distribution principles. At 28 μs with complete explosive detonation, the jet propagates axially while clearly exhibiting the PER theory predicted velocity gradient. When approaching the steel target at 36 μs, the elongating jet maintains structural integrity with its head velocity significantly exceeding slug velocity and no fracture occurring prior to impact.

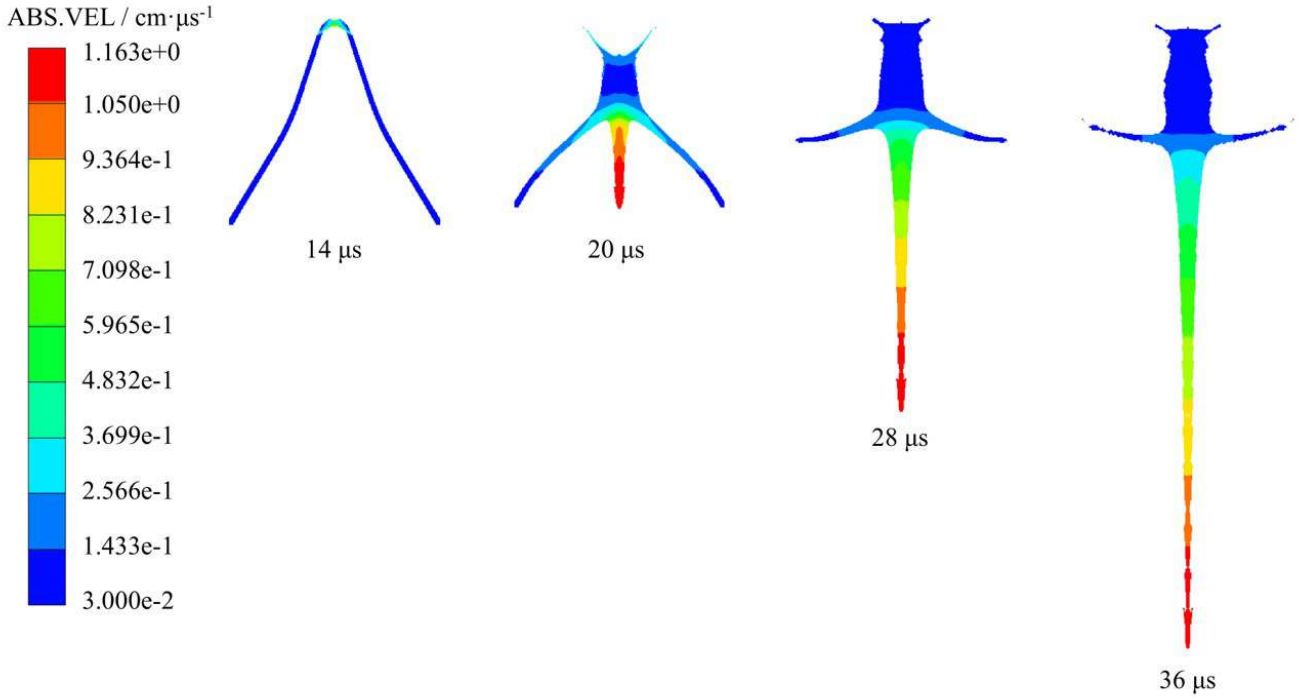


Figure 13 Formation and stretching process of the shaped charge jet

The penetration process of a shaped charge jet into a steel target is illustrated in Figure 14. At 37 μs, when the jet tip contacts the steel target surface, extreme pressure is generated at the impact point due to the jet's high velocity. According to hydrodynamic principles, this high-speed collision induces intense shock waves that propagate rapidly into the target while exerting reactive forces on the jet tip. During this phase, the jet tip initiates compressive deformation of the target surface material. At 150 μs, distinct jet fracture occurs. The high-pressure, high-velocity jet continuously compresses and shears the target material, predominantly inducing plastic deformation. Target material surrounding the jet tip flows radially outward, forming a "penetration channel" with a smooth inner wall in the front section and a "gourd-shaped" morphology in the rear. This wall morphology is intrinsically linked to the velocity characteristics of the jet. During the initial penetration phase, the jet velocity significantly surpasses the target material's plastic flow velocity, thereby sustaining continuous penetration even under persistent resistance conditions, forming the smooth front section. However, as the velocity gradient within the jet intensifies, tensile fracture occurs, causing the jet to break into discrete segments. These fragmented jet segments successively create new penetration cavities along the axis, ultimately generating the characteristic "gourd-shaped" wall morphology in the rear section. At 300 μs, the channel diameter gradually diminishes as jet energy dissipates, accompanied by significantly reduced tip velocity and pressure. During this stage, the slug contributes to target damage through hole expansion effects. At 600 μs, penetration terminates as jet

energy exhausts and velocity drops below the threshold for continued advancement. The results demonstrate the formation of a deep penetration cavity in the semi-infinite steel target.

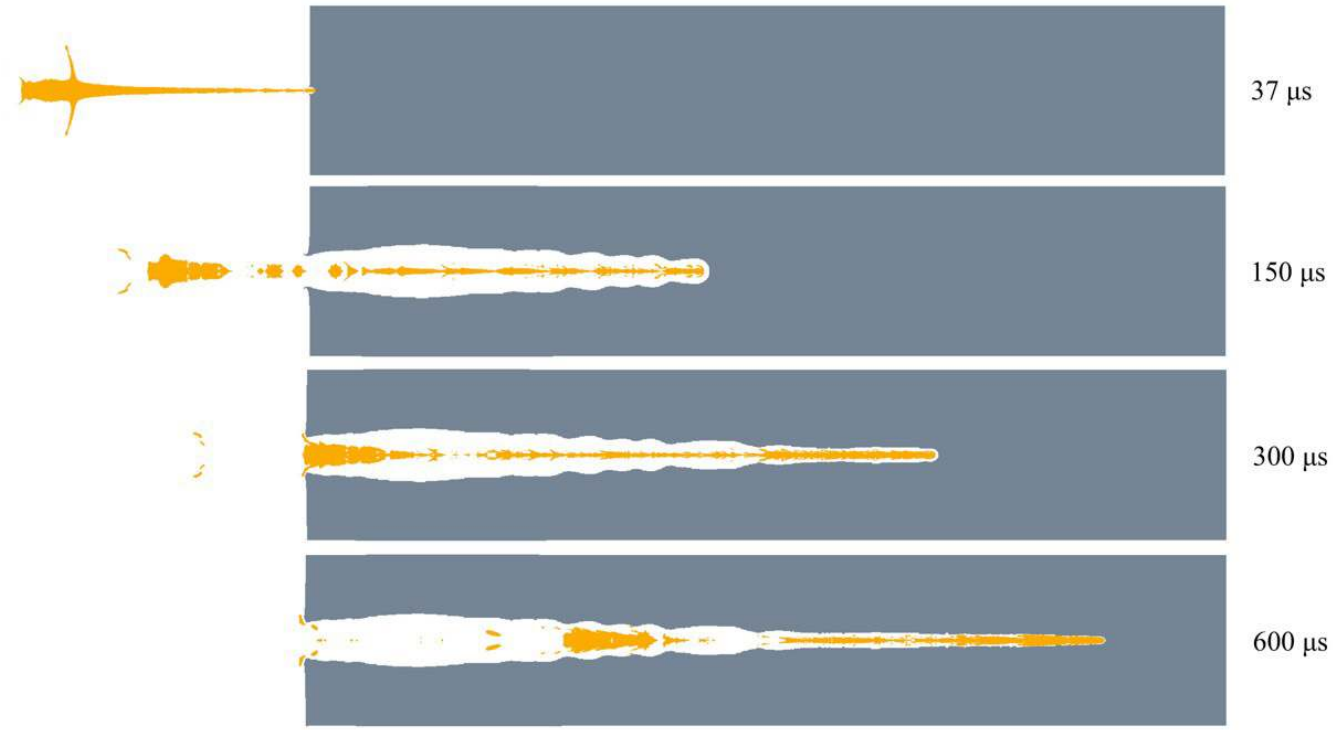


Figure 14 Penetration process of the shaped charge jet into the steel target

3.3.3 Comparative analysis

To further demonstrate the advantages of electroformed nanocrystalline copper liners over conventionally manufactured coarse-grained copper liners in terms of penetration performance, numerical simulations were conducted to compare differences in jet formation and penetration behavior. Numerical models of identical dimensions were established, with the liner material selected as oxygen-free copper from reference (Tang et al. 2025), and relevant parameters are listed in Table 8.

Table 8 Material parameters of oxygen-free copper (Tang et al. 2025)

ρ/g·cm^{-3}	A/MPa	B/MPa	n	C	m	C_0/km·s^{-1}	S	γ	T_{melt}/K
8.93	90	292	0.31	0.025	1.09	3.94	1.489	2.02	1790

Figure 15 compares the jet formation effects and axial velocity distributions of nanocrystalline copper and coarse-grained copper liners at identical time points. At 36 μs, neither jet has initiated penetration into the steel target, with both maintaining uniform morphology and no observed fracture. In terms of jet formation, the diameters of the jet tips for both are around 0.24 cm, the diameters of the slugs are around 1.56 cm, and the jet lengths are approximately 22.00 cm. Velocity distribution analysis reveals tail velocities of 974 m·s^{-1} for the nanocrystalline copper jet and 1030 m·s^{-1} for the coarse-grained copper jet, with tip velocities reaching 11590 m·s^{-1} and 11461 m·s^{-1}, respectively. The velocity at the jet-slug interface measures 464 m·s^{-1} for nanocrystalline copper and 438 m·s^{-1} for coarse-grained copper. Notably, the higher tip velocity and lower tail velocity of the nanocrystalline copper jet enhance its stretching capability, thereby improving penetration performance.

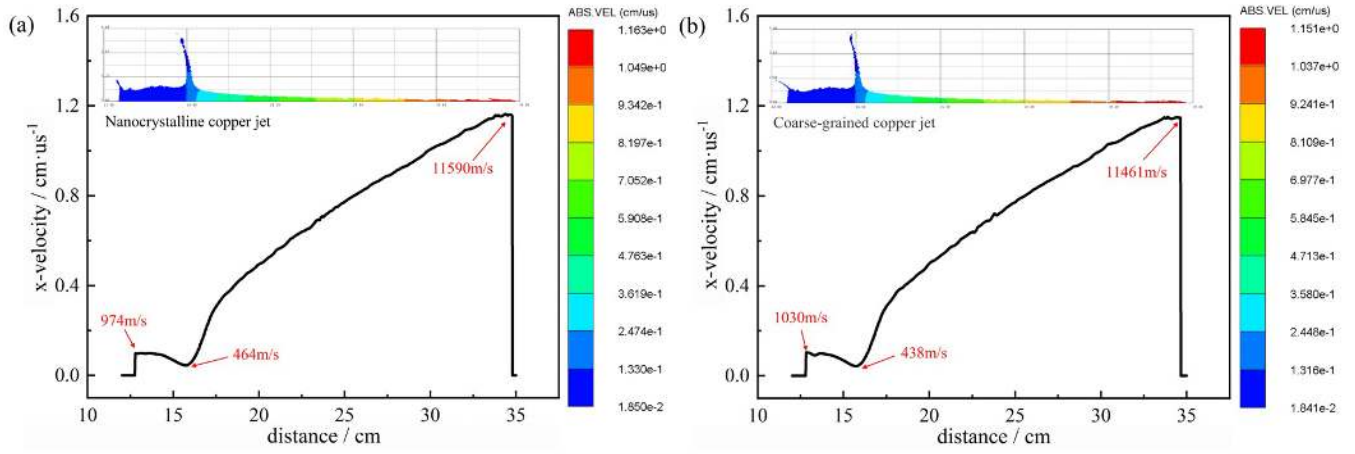


Figure 15 Jet formation and velocity distribution at 36 μs: (a) nanocrystalline copper; (b) coarse-grained copper

Since the jet does not fracture before penetrating the steel target, in order to investigate grain size effects on jet fracture timing, simulations of jet formation without target interaction were conducted. As shown in Figure 16, at 39 μs, the nanocrystalline copper jet remains intact under stretching, while the coarse-grained copper jet fractures due to pronounced velocity gradients. This demonstrates that reduced grain size effectively delays jet fracture.

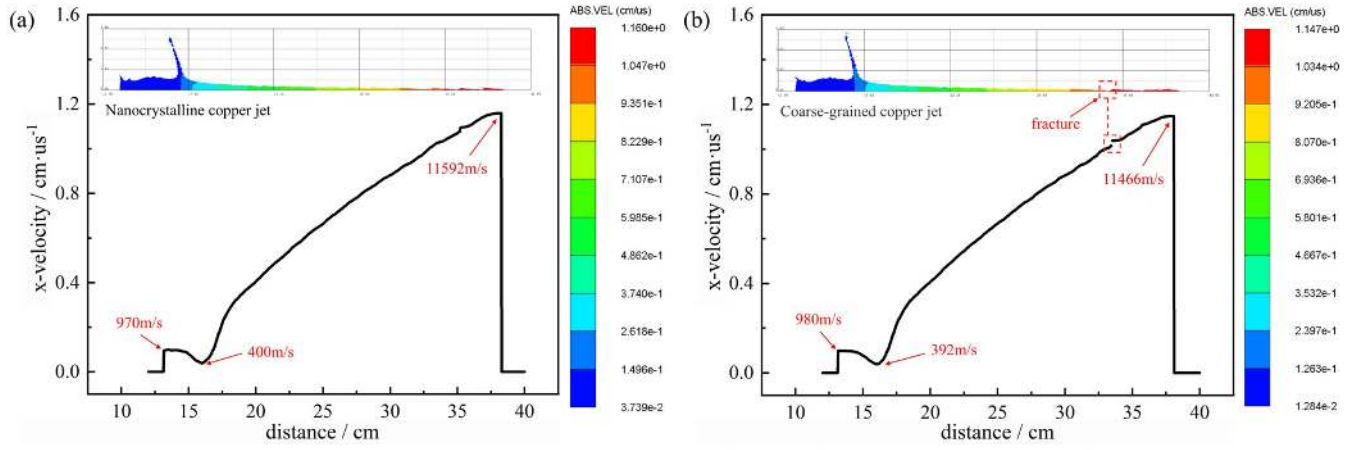


Figure 16 Jet formation and velocity distribution at 39 μs: (a) nanocrystalline copper; (b) coarse-grained copper

Typically, the jet fractures first at or near its head, leading to the formation of a fractured zone (Z_F) where the jet breaks into numerous small segments. As the jet continues to stretch forward, the fracture front propagates continuously toward the tail, resulting in the backward expansion of the fractured zone. The region between the fracture front and the tail, where the material remains continuous and intact, is termed the continuous zone (Z_C). In this study, the degree of jet fracture is quantified by the expression $D = Z_F / (Z_F + Z_C) \times 100\%$. As the jet continues to stretch forward, the fracture behavior of the nanocrystalline copper jet and the coarse-grained copper jet differs. As shown in Figure 17, at 45 μs, the nanocrystalline copper jet fractures once, while the coarse-grained copper jet fractures twice. At 50 μs, multiple fractures occur in the jet. Specifically, the nanocrystalline copper jet fractures three times, with the fractured zone accounting for 18% of the total zone. The coarse-grained copper jet fractures four times, with the fractured zone accounting for 32% of the total zone. The fracture range of the coarse-grained copper jet is significantly higher than that of the nanocrystalline copper jet. For pure copper materials, grain refinement can significantly enhance their strength, thereby improving the material's resistance to deformation under external loads. During the jet formation process in shaped charge liners, where materials undergo high-strain-rate deformation, grain-refined pure copper exhibits superior deformation resistance. This enables prolonged maintenance of jet integrity and delays the onset of tip fragmentation.

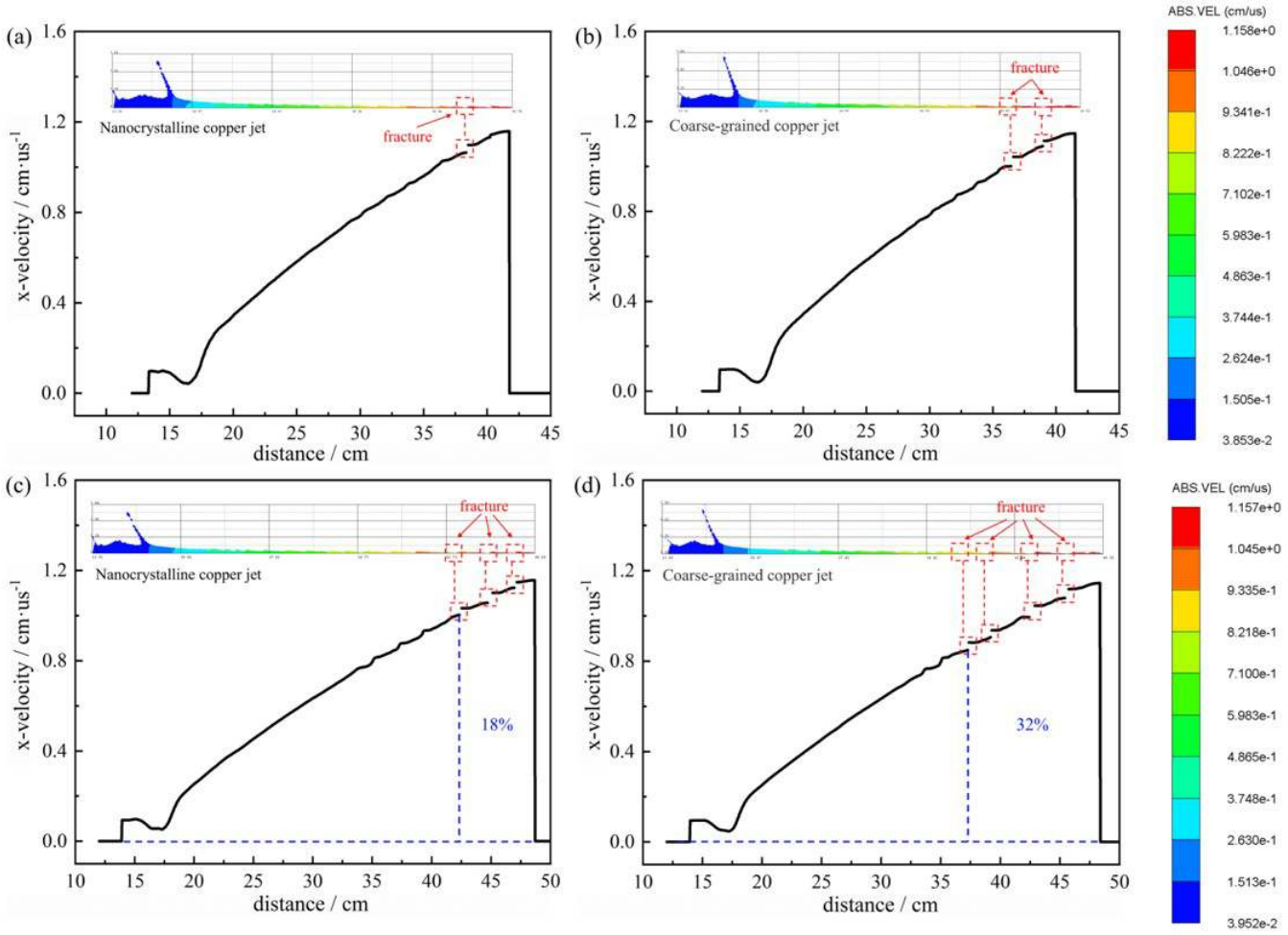


Figure 17 Jet formation and velocity distribution: (a) nanocrystalline copper at 45 μs; (b) coarse-grained copper at 45 μs; (c) nanocrystalline copper at 50 μs; (d) coarse-grained copper at 50 μs

The superplasticity of shaped charge jets originates from dynamic recrystallization that occurs under high temperature and high strain rate conditions. Dynamic recrystallization is a recrystallization phenomenon that occurs in materials under high strain rate or high temperature conditions. Its essence is a competitive process between dislocation multiplication and grain boundary migration, which replaces deformed structures by forming new grains (Liu et al. 2024, Li et al. 2023). Grain refinement significantly promotes dynamic recrystallization by reducing critical strain and increasing the nucleation site density of defects such as grain boundaries or twin boundaries. For example, the yield strength of electroformed nanocrystalline copper can reach 250 MPa. Its high-density grain boundaries and coherent twin boundaries not only enhance strength but also provide preferential nucleation sites for dynamic recrystallization by reducing the mean free path of dislocations and enhancing dislocation storage capacity (Yang et al. 2025, Li et al. 2025). During jet formation in shaped charge liners, dynamic recrystallization maintains the plastic flow capacity of the material through the balance of dynamic softening and work hardening, thereby extending the jet length. Due to the fine grains of the nanocrystalline copper liner, dynamic recrystallization occurs easily and rapidly, so the jet can maintain integrity and consistency for a longer time. In contrast, due to the larger grains of the coarse-grained copper liner, dynamic recrystallization is difficult to occur or occurs slowly. Therefore, the jet head fractures in a short time, and the fracture range expands significantly with time.

Based on the significant differences in dynamic tensile and fracture characteristics between coarse-grained and nanocrystalline copper jets, a comparative analysis was conducted on their energy transfer efficiency and channel morphological features during steel target penetration. As shown in Figure 18, the morphological characteristics of penetration cavity during shaped charge jet penetration into steel targets can be divided into three typical stages according to jet dynamic behavior, with their formation mechanisms closely related to the jet's continuity state and energy transfer modes. The initial continuous jet penetration stage corresponds to the high-speed continuous state of the unbroken jet head. At this stage, jet energy is primarily transferred along the penetration direction (axial direction)

with minimal energy dissipation perpendicular to it (radial direction), forming large-diameter channels with smooth pore walls. The fractured jet penetration stage occurs as velocity gradients cause jet fragmentation. Discrete jet fragments intermittently impact the steel target, resulting in un-concentrated axial energy distribution and significantly increased radial energy dissipation. This expands channel diameter while reducing axial penetration capability, and the alternating axial impact and radial hole enlargement form locally "gourd-shaped" channels. The cumulative jet penetration stage begins when discrete jet fragments aggregate toward the channel base to form a cumulative jet. Thermal softening of the steel target occurs due to accumulated thermal effects from prior penetration, reducing target strength and enabling continuous compaction of the channel base by momentum transfer. The process terminates when kinetic energy becomes insufficient to overcome target strength.

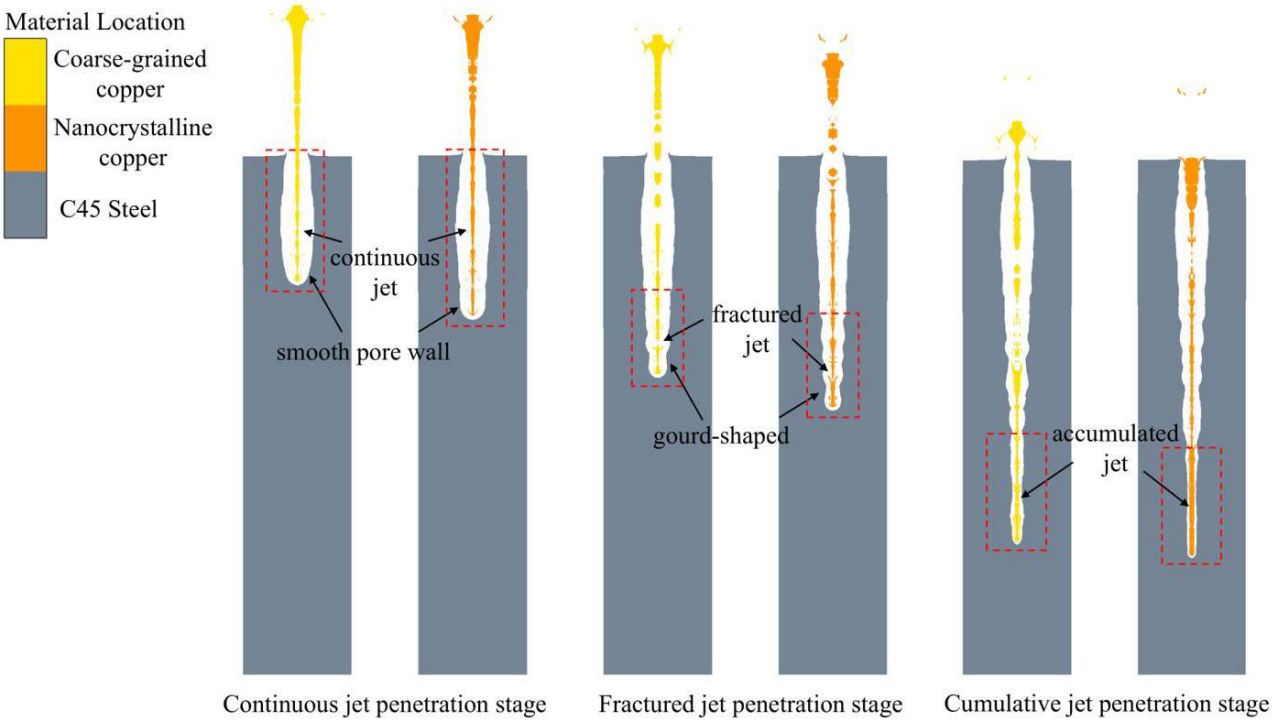


Figure 18 Comparison of penetration process

Under identical charge configurations and standoff distances, the numerical simulation results of the coarse-grained copper jet penetration were compared with the penetration cavity morphology of the nanocrystalline copper jet, as shown in Figure 19. It can be concluded that the penetration depth of the nanocrystalline copper jet is 608.0 mm, with an entrance diameter of 32.4 mm and an exit diameter of 9.0 mm at the 500 mm depth of the steel target. In contrast, the penetration depth of the coarse-grained copper jet is 520.0 mm, with an entrance diameter of 31.8 mm and an exit diameter of 11.4 mm at the same target depth. The comparison between the numerical simulation and experimental results is presented in Table 9. The error values for the average penetration depth, average entrance diameter, and average exit diameter of the nanocrystalline copper jet are 3.3%, 3.3%, and 5.3%, respectively. For the coarse-grained copper jet, the corresponding error values are 0.3%, 9.1%, and 8.6%, respectively. The results show that the experimental and numerical simulation results are in excellent agreement, indicating that the material, geometric, boundary condition, and other model settings and parameters in the numerical simulation are correct and can accurately describe the actual physical process.

Table 9 Comparison between experimental and simulated penetration results

No.	D_{en}/mm		D_{ex}/mm		P/mm	
	experiment	simulation	experiment	simulation	experiment	simulation
I	34.0	32.4	8.9	9.0	583.0	608.0
II	33.0		8.2		594.0	
III	43.0	31.8	12.0	11.4	515.0	520.0
IV	27.0		9.0		522.0	

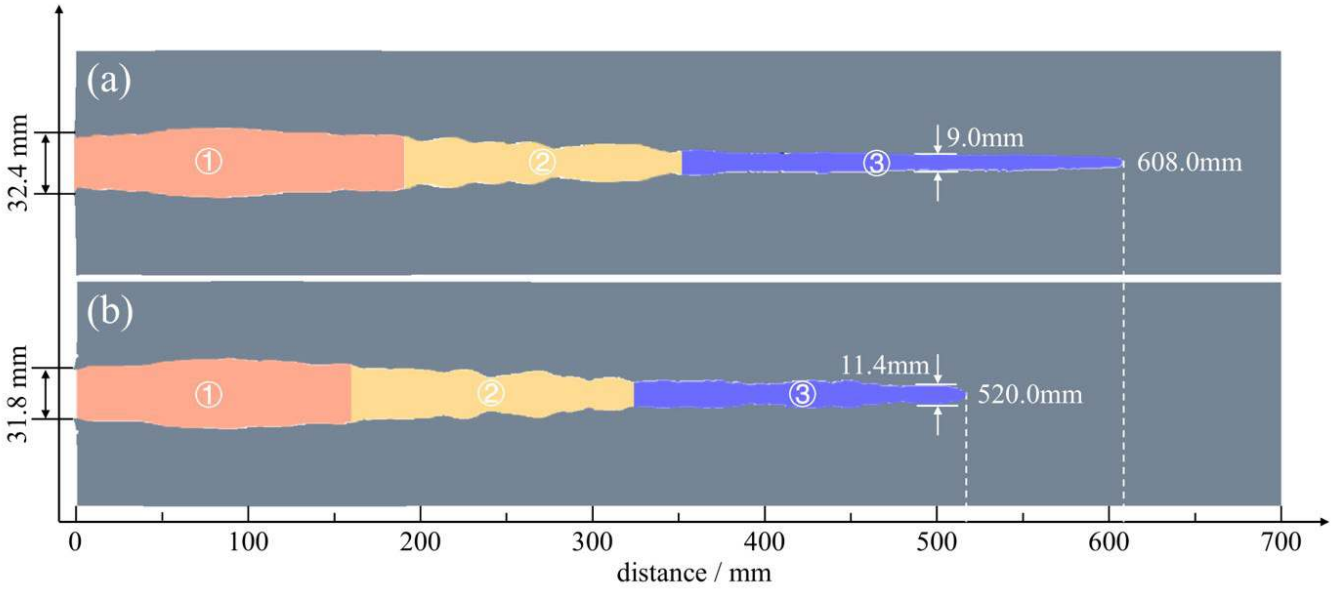


Figure 19 Comparison of penetration cavity morphologies: (a) nanocrystalline copper; (b) coarse-grained copper

According to the distinct effects of the jet on the internal steel target across the three typical stages in Figure 18, the penetration cavity morphology was divided into three regions: ①, ②, and ③. Region ① had the largest average penetration diameter with a smooth pore wall; region ② had a moderate average penetration diameter with a rougher pore wall, exhibiting a "gourd-shaped" appearance; and region ③ had the smallest average penetration diameter with a relatively smooth pore wall. The region ① of the nanocrystalline copper jet was significantly larger than that of the coarse-grained copper jet, indicating that the nanocrystalline copper jet fractured later during the penetration process. Region ② was smaller than that of the coarse-grained copper jet, indicating that the fracture extent was smaller during the penetration process. Due to the differences in fracture time and fracture extent, the final penetration abilities of the jets were significantly different. Region ③ was much larger than that of the coarse-grained copper jet, indicating that the penetration ability of the nanocrystalline copper jet was higher than that of the coarse-grained copper jet. From the perspective of the penetration process, these results were consistent with the previous analysis of the jet formation.

4 CONCLUSIONS

This study fabricated nanocrystalline copper tensile specimens and liners via electroforming. Quasi-static tensile tests, split Hopkinson tensile bar tests, and static penetration experiments were conducted. Johnson-Cook constitutive parameters were fitted based on experimental data, and a dynamic response model of liners under explosive loading was established using AUTODYN software. Combining experiments and simulations, the jet formation and penetration effects of electroformed nanocrystalline copper liners were investigated. The main conclusions are as follows:

(1) Quasi-static and dynamic tensile tests of nanocrystalline copper specimens show this material possesses higher strength, good plasticity, and significant strain rate strengthening effects. Its yield strength is 1.78 times that of coarse-grained copper.

(2) Comparative static penetration experiments reveal significantly improved penetration performance of nanocrystalline copper liners over coarse-grained copper liners, with average penetration depth increasing by 13.5%.

(3) Numerical simulations demonstrate under identical charge configurations, nanocrystalline copper jets initiate fracture at 45 microseconds, 15.4% later than coarse-grained copper jets, maintaining extended jet integrity. Simulated penetration results for nanocrystalline copper liners show less than 5.3% error compared with experimental averages. This validates the accuracy of the Johnson-Cook model fitting and rationality of material parameter selection, providing essential foundations for subsequent optimization of nanocrystalline copper liners.

Acknowledgments

The authors would like to acknowledge QinChuangyuan Project of Shaanxi Province (No. QCYRCXM-2022-153 and No. QCYRCXM-2023-032).

Author's Contribuitions: Methodology, Azhen Zhang, Rongxin Li, Yuchun Li and Bo Zhou; Conceptualization, Yuchun Li; Investigation, Azhen Zhang, Rongxin Li, Ruiqi Wang, Yuchun Li and Bo Zhou; Writing - original draft, Azhen Zhang; Writing - review & editing, Rongxin Li, Ruiqi Wang and Yuchun Li; Funding acquisition, Longfei Xie, Yuchun Li and Bo Zhou; Data curation, Longfei Xie and Bo Zhou; Software, Azhen Zhang, Rongxin Li and Yuchun Li, Supervision, Junyi Huang, Zhenru Gao and Yuchun Li

Data availability: Research data is available in the body of the article

Editor: Marcílio Alves

References

Wang Y T, Huang Z X, Zu X D, et al. (2021) Experimental study on jet formation and penetration characteristics of square cross-section shaped charge. Latin American Journal of Solids and Structures 18(5): e379.

Chen P, Li W B, Li Y M, et al. (2024) Formation of explosively-formed projectile with tail fins using polygonal charges. Latin American Journal of Solids and Structures 21(1): e516.

Liu J, Jian Y L, Chen Y L, et al. (2023) Shock vibration response characteristic of perforating tubing string in ultra-deep wells. Geoenergy Science and Engineering 228: 212008.

Chai Y B, Luo N, Zhang H H, et al. (2023) Application of controlled blasting demolition technology in ultra-high coaxial thin-walled steel inner cylinder reinforced concrete chimney. Case Studies in Construction Materials 18: e01936.

Golaski S K. (1987) Effect of liner grain size on shaped charge jet performance and characteristics: BRL-TR- 2800. Aberdeen, MD: US Army Ballistic Research Laboratory.

Bourne B, Jones P N, Warren R H. (1993) Grain size and crystallographic texture effects on the performance of shaped charge 14th Internatioanl Symposium on Ballistics. Quebec, Canada: IBC: 119-124.

Wang T F, Wang L, Ruan W J, et al. (1996) The effects of the grain size of a liner on the performance of shaped charge jets. Chinese Journal of High Pressure Physics 10(4): 52-56+58-59.

Huang Y J, Li X H, Zhao F, et al. (2016) One new method for preparing nanocrystalline metal. Materials Letters 166: 78-80.

Ebrahimi G R, Barghamadi A, Ezatpour H R, et al. (2019) A novel single pass severe plastic deformation method using combination of planar twist extrusion and conventional extrusion. Journal of Manufacturing Processes 47: 427-436.

Jiang J Y, Du J H, Yan J K, et al. (2022) Preparation of $Al_xCuFeNiCoCr$ high entropy alloy by powder metallurgy method and its properties. Rare Metal Materials and Engineering 51(2): 392-399.

Ye Z X, Wang T, Wu S, et al. (2017) Na-doped ZnO nanorods fabricated by chemical vapor deposition and their optoelectrical properties. Journal of Alloys and Compounds 690: 189-194.

Xiao M, Song Z Y, Gao X F, et al. (2025) Regulation of the surface morphology of $CoNiSe_2$ by magnetron sputtering of Au nanoparticles for the property-promotion of electrode materials for high-performance supercapacitors. Journal of Alloys and Compounds 1035: 181452.

Zhou B, Su B, Li M, et al. (2021) A comparative study of Ni75Fe25 microcomponents fabricated by microelectroforming and micromolding. Journal of Materials Processing Technology 290: 116997.

Sun Q. (1992) Domestically first developed electroforming technology for shaped charge liners (Part 2). Modern Weaponry (12): 11-15.

Wang Z H. (2012) Effective Methods to Enhance the Power of Shaped Charge Warheads: Precision Electroforming Technology for Copper Liners, In National Defense Science and Technology Industry Center for Research and Application of Automated Ammunition Loading Technology, Ordnance Equipment Committee of the China Ordnance Society: 130-132.

Sun Q. (2000) A review on the progress of research in electroformed liners. Acta Armamentarii 21(S1): 86-88.

Lei W N, Zhu D. (2003) Study on nanocrystalline electroforming process. China Mechanical Engineering (12): 82-85+7.

Lei W N, Zhu Z W, Tao G. (2010) Experimental research on finer-grain electroformed nickel shaped charge liner. China Mechanical Engineering 21(3): 340-343.

Li C H, Cheng S W, Wang L, et al. (2009) Microstructure and texture in nickel shaped charge liner prapared by electroformation from sulfamate. Ordnance Material Science and Engineering 32(6): 7-10.

Li C H, Cheng S W, Wang L, et al. (2011) High speed deformation behavior of the electroformed nickel liner of shaped charge. Journal of University of Science and Technology Beijing 33(1): 53-58.

Tian W H, Fan A L, Gao H Y, et al. (2003) Comparison of microstructures in electroformed copper liners of shaped charges before and after plastic deformation at different strain rates. Materials Science and Engineering: A 350(1-2): 160-167.

Fan A L, Li S K, Tian W H, et al. (2007) Comparison of microstructures in electroformed and spin-formed copper liners of shaped charge undergone high-strain-rate deformation. Transactions of Nonferrous Metals Society of China 17(6): 1447-1450.

Fan A L, Li S K, Tian W H. (2008) Grain growth and texture evolution in electroformed copper liners of shaped charges. Materials Science and Engineering: A 474(1-2): 208-213.

Yang F, Li C H, Cheng S W, et al. (2010) Deformation behavior of explosive detonation in electroformed nickel liner of shaped charge with nano-sized grains. Transactions of Nonferrous Metals Society of China 20(8): 1397-1402.

Tamer E, Salah S, Ahmed H. (2017) Influence of electric current intensity on the performance of electroformed copper liner for shaped charge application. Defence Technology 13(6): 439-442.

Huang B Y, Xiong W, Zhang X F, et al. (2021) Experimental study on jet formation and penetration performance of double-layered reactive liners with k-charge. Chinese Journal of Energetic Materials (Hanneng Cailiao) 29(2): 149-156.

Li J, Luo K, An Q. (2025) Unraveling the Hall-Petch to inverse Hall-Petch transition in nanocrystalline CdTe. International Journal of Mechanical Sciences 286: 109852.

Lei W N, Zhu D, Qu N S. (2004) Research on mechanical properties of nanocrystalline electroforming layer. Chinese Journal of Mechanical Engineering 40(12): 124-127.

Wang J, Li N, Anderoglu O, et al. (2010) Detwinning mechanisms for growth twins in face-centered cubic metals. Acta Materialia 58(6): 2262-2270.

Huang X Y, Tao J L. (2016) Tensile mechanical properties research of three construction steel bars in high strain rate. Engineering Mechanics 33(07): 184-189.

Zaretsky E B. (2025) Temperature effect on austenite–martensite transformation in shock-loaded pseudoelastic nitinol. Journal of Applied Physics 137(13): 135902.

Li N, Chen J W, Qu J L, et al. (2024) Flow behavior and microstructure evolution of FGH95 alloy formed by vacuum powder forging. Journal of Aeronautical Materials 44(2): 133-142.

Li R X, Wang R Q, Tian Q W, et al. (2024) An investigation on the jet formation and penetration characteristics of the CuCoCrFeNi high-entropy alloy liner. AIP Advances 14(5): 055017.

Gao Y X, Ji C, Wang X, et al. (2024) Oblique penetration performance of Explosively Formed Projectile (EFP) on 6061 aluminum target: experiments and simulations. Latin American Journal of Solids and Structures 21(1): e515.

Li R X, Ding J B, Zhao Y Y, et al. (2024) Preliminary study on the dynamic deformation mechanism of CoCrFeNi high-entropy alloy and its application in the shaped charge liner. Journal of Alloys and Compounds 999: 175083.

Dou Y P, Liang Z F, Dou J H. (2025) Damage Laws of Large-Sized Multimedium Materials by Shaped Charge Jets. Latin American Journal of Solids and Structures 22(3): e8386.

Yan C, Huang Z X, Zu X D, et al. (2017) Mechanical property of ultra-fine grained copper material and study on application of liner field. Journal of Ballistics 29(1): 85-92.

Guo H G, Zheng Y F, Yu Q B, et al. (2019) Penetration behavior of reactive liner shaped charge jet impacting thick steel plates. International Journal of Impact Engineering 126: 76-84.

Hong B H, Li W B, Li Yi M, et al. (2024) Jet formation and penetration performance of a double-layer charge liner with chemically-deposited tungsten as the inner liner. Defence Technology 33: 374-385.

Zhang C P, Zhang X F, Tan M T, et al. (2023) Experimental and numerical simulation of shaped charge jet penetrating concrete and rock targets. Chinese Journal of Energetic Materials (Hanneng Cailiao) 31(8): 773-785.

Pugh E M, Eichelberger R J, Rostoker N. (1952) Theory of jet formation by charges with lined conical cavities. Journal of Applied Physics 23(5): 532-536.

Tang W J, Ji C, Wang Y T, et al. (2025) The influence of stand-off distance on the penetration characteristics of Toroidal Explosively Formed Projectile (TEFP). Latin American Journal of Solids and Structures 22(2): e8415.

Liu W H, Liu F X, Xie G L, et al. (2024) Effect of nano-scaled Al_2O_3 particles on dynamic recrystallization behavior and microstructure evolution of pure copper in hot deformation. Materials Science and Engineering: A 914: 147123.

Li J W, Du Z H, Wang M C, et al. (2023) Planar fault assisted dynamic recrystallization in copper during high-velocity impacts. Journal of Applied Physics 133 (24): 245101.

Yang H B, Li S, Wang S, et al. (2025) The microstructure, texture and grain refinement mechanism of cold-rolled AlNdTi alloy target: Large deformation promotes dynamic recrystallization. Intermetallics 182: 108761.

Li D Z, Zhao X M, Zhang H L, et al. (2025) Flow stress-strain curves and dynamic recrystallization behavior of high carbon low alloy steels during hot deformation. Journal of Materials Research and Technology 35: 3144-3160.